

ORIGINAL RESEARCH ARTICLE

Build orientation-dependent evolution of residual stress, crystallographic texture, and mechanical anisotropy in laser powder bed-fused IN625

Sheeza Khan¹ and A. Raja Annamalai^{2*} 

¹School of Mechanical Engineering, Vellore Institute of Technology, Vellore, Tamil Nadu, India

²Centre for Innovative Manufacturing Research, Vellore Institute of Technology, Vellore, Tamil Nadu, India

Abstract

The mechanical anisotropy of laser powder bed-fused IN625 necessitates consideration of build orientation, as inherent directional solidification during additive manufacturing induces mechanical anisotropy and affects grain morphology, texture evolution, and mechanical behavior, thereby requiring an orientation-specific evaluation to optimize structural integrity. This paper presents the structure–property relationships of as-built specimens fabricated in three distinct build orientations. To assess orientation-dependent effects, tensile specimens were printed in three build orientations: 0°, 45°, and 90°. Grain morphology, grain size distribution, and microstructural variation were investigated using electron backscatter diffraction. The statistical distribution of grain orientation and pole figure analysis revealed significant textural variation and directional dependence, consistent with anisotropic behavior. The findings demonstrate that build orientation significantly influences the structural integrity of laser powder bed-fused IN625 components. Among the examined orientations, the 0° condition exhibits a pronounced <001> texture aligned with the build direction. Pole figure and orientation distribution function analyses confirm a dominant cube texture at 0°, which transitions to a cube–goss texture at 45°. Mechanical testing corroborates the electron backscatter diffraction results, with the 0° orientation exhibiting the highest yield strength (727 MPa) and ultimate tensile strength (963 MPa), attributed to a favorable alignment of load-bearing grains. Residual stress-assisted characterization indicates that nominal in-plane compressive stresses predominate in the 0° orientation.

*Corresponding author:

A. Raja Annamalai
(raja.annamalai@vit.ac.in)

Citation: Khan S, Annamalai AR. Build orientation-dependent evolution of residual stress, crystallographic texture, and mechanical anisotropy in laser powder bed-fused IN625. *Mater Sci Add Manuf.* 2026;5(2):026040007. doi: 10.36922/MSAM026040007

Received: January 21, 2026

Revised: February 20, 2026

Accepted: March 2, 2026

Published online: May 25, 2026

Copyright: © 2026 Author(s). This is an Open Access article distributed under the terms of the Creative Commons Attribution License, permitting distribution, and reproduction in any medium, provided the original work is properly cited.

Publisher's Note: AccScience Publishing remains neutral with regard to jurisdictional claims in published maps and institutional affiliations.

Keywords: Additive manufacturing; Laser powder bed fusion; IN625; Residual stress; Crystallographic texture; Orientation studies

1. Introduction

Additive manufacturing (AM) has ushered in the next industrial revolution.¹ Since its inception in 1980, AM has expanded its capabilities, enabling greater complexity, customization, and consolidation.² With its role in rapid prototyping firmly established, the technology demonstrates a compelling capacity to transform a broad spectrum of industrial sectors. It has gained particular prominence in the aerospace sector for

producing lightweight engine components, enhancing the buy-to-fly ratio. AM contrasts sharply with traditional manufacturing processes in terms of waste reduction, labor intensity, and lead time.³

Metal AM technology has advanced remarkably in producing complex designs. It is a process that builds parts and components layer by layer.⁴ Emerging industrial advancements have driven demand for metallic materials with superior strength and ductility. The high demand for high-temperature operational components in various applications has made nickel-based superalloys preferred materials.⁵ Nickel and titanium alloys are among the most widely used materials in metal AM.⁶

Metal AM is generally referred to as a rapid solidification process. Rapid solidification, with a cooling rate of $\sim 10^6$ K/s and a high temperature gradient ($\sim 10^5$ K/m), results in non-equilibrium microstructures.^{7,8} The material response to rapid heating and cooling produces fine microstructures, while the direction of heat flow leads to columnar structures.^{9,10} The G/R ratio, where G is the temperature gradient and R is the solidification rate, governs microstructure evolution and defect formation.^{11,12} As reported by Wei *et al.*¹³, solidification morphology depends on this critical parameter (G/R ratio), leading to four distinct microstructural regimes. Notably, with increasing R, a planar structure forms initially, followed by cellular, columnar, and equiaxed transformations¹⁴, which contribute to improved mechanical properties due to microstructural refinement.

Powder-based technologies adhering to American Society for Testing and Materials (ASTM) standards, particularly powder bed fusion–laser based (PBF-LB), are prone to residual stress generation.¹⁵ Large thermal gradients, a primary driver of these stresses, are inherent to metal AM and can be controlled via processing parameters. Short interaction times and localized heat input primarily induce these stresses.¹⁵ Processing parameters further influence the evolution of residual stresses.¹⁶ The residual stress evolution model proposed by Mercelis *et al.*¹⁷ describes the mechanism responsible for stress development during the cool-down phase.¹⁸ The laser powder bed fusion process enables the production of intricate geometries and integrated functions in a single build, eliminating the need for secondary machining.¹⁹

In this context, the present study investigates the complex process–structure–property (PSP) relationships associated with this AM process. Powder is most commonly used as a feedstock in AM processes, which are typically selective melting processes employing a focused heat source, such as a laser, to consolidate the melt during subsequent

cooling and form a component²⁰, thereby producing near-net-shaped specimens with high density.²¹ PBF-LB gives rise to an as-built microstructure characterized by rapid solidification, compositional inhomogeneity, and inherent residual stress development. Furthermore, the energy input is quantified through energy density parameters (i.e., laser energy density and volumetric energy density), which affect melt pool dynamics, material densification, and consequently the microstructure and mechanical performance of the additively manufactured component.²² These energy densities can be calculated as follows²³:

$$\text{Laser energy density: } \frac{J}{mm^2} = \frac{\text{Power (W)}}{\text{Scanspeed} \left(\frac{mm}{s} \right) / \text{beam diamter (mm)}} \quad (1)$$

$$\text{Volumetric energy density: } \frac{J}{m^3} = \frac{\text{Power(w)}}{v * h * t} \quad (2)$$

where v is the scan speed, h is the hatch spacing, and t is the layer thickness.

Literature highlights the importance of build orientation studies²⁴, as the anisotropic microstructure developed during AM leads to directionally aligned grain textures within the material.^{25,26} Building upon these studies, the central objective of the present study is to apply the PSP framework, focusing on how different build orientations influence microstructural evolution and, consequently, the mechanical performance of the additively manufactured component.²⁷ Notably, processing parameters, microstructural features, and material properties constitute the core elements of the PSP model.²³ The evaluation of IN625 strength is based on residual stress analysis combined with electron backscatter diffraction (EBSD) characterization, which measures geometrically necessary dislocation (GND) density and kernel average misorientation (KAM) distribution within the grains at different build orientations. UNS00625 components have predominantly been investigated with emphasis on two build orientations (perpendicular and parallel).²⁸

The present study extends prior investigations by systematically evaluating three build orientations within the PSP framework. Optimization of the build orientation is performed using three variants. By integrating EBSD-based texture quantification, X-ray residual stress analysis, and uniaxial tensile testing, this study elucidates orientation-dependent anisotropy by correlating crystallographic texture and stress state with the macroscopic mechanical response. Compressive residual stresses, grain orientation relative to the build direction, and EBSD-derived dislocation density collectively contribute to enhanced yield and tensile strength.

2. Materials and methods

2.1. Printing description

An EOS M 290 AM system (Germany) with a ytterbium fiber laser was used to print the tensile specimens according to ASTM E8 standards. Process parameters are listed in Table 1.

The gas-atomized powder was spherical, and its chemical composition was analyzed using energy-dispersive spectroscopy (Oxford Instruments). The average particle size was 35 μm , measured using scanning electron microscopy (SEM; Thermo Fisher (FEI QUANTA 250 FEG), USA). The D_{10} , D_{50} , and D_{90} values of the feedstock powder were 20 μm , 30.3 μm , and 49.5 μm , respectively, in accordance with ASTM B822. Specimens were fabricated using a laser power of 400 W, a scanning speed of 910 mm/s, and a layer thickness of 60 μm . The relative density was determined to be 98% according to Archimedes' principle for the cubic-oriented specimens prepared for EBSD analysis (dimensions = 10 \times 10 \times 3 mm³).

Microstructural analysis was conducted using a field emission scanning electron microscope equipped with an Oxford Instruments EBSD detector. Electropolishing was performed prior to scanning using a solution containing perchloric acid and methanol in a 20:80 vol% ratio at 12 V. Mapping was performed with a step size of 0.5 μm , and the accelerating voltage was set to 20 kV. The acquired data were analyzed using MTEX software.²⁹ The selected EBSD scan area was 300 \times 300 μm^2 along the building direction for the three orientation variants. Flat subsize tensile specimens were prepared according to ASTM E8/8M (overall length = 100 mm; gauge length = 25 mm; thickness = 10 mm; width = 6 mm; reduced section length = 32 mm; fillet radius = 6 mm).

2.2. Residual stress quantification

Residual stress was measured using the $\sin^2\psi$ method by X-ray diffraction (a non-destructive technique) using a PAN Analytical X'pert PRO XRD system (PAN Analytical XRD (Netherlands) with a Cu K α source. The surface residual stress of electropolished specimens was compared for the three build orientations. The magnitude of residual stresses was determined at three azimuth angles ($\varphi = 0^\circ$, 90° , and 135°) relative to the build orientation. Measurements were performed using the standard $\sin^2\psi$ method to determine the diffraction-averaged stress within the near-surface region, corresponding to a shallow penetration depth of approximately 5–10 μm . The (311) diffraction peak was selected due to its high diffraction intensity. The peak was segmented into 10 points; five positive and five negative tilt angles were recorded. A condition of plane stress

exists in the thin diffracting surface; thus, no normal or shear stresses are acting out of the free surface. Therefore, the stresses of interest in the plane of the surface can be determined without reference to an unstressed lattice spacing standard.³⁰ In this conventional method, a zero slope of the least-squares regression line (i.e., the observed change in interplanar spacing is zero) indicates strain-free atomic planes, and the corresponding interplanar spacing can be considered the stress-free lattice spacing. Normal and shear stresses were considered in the analysis. The X-ray beam was rotated at all three angles to evaluate all the stress tensor components.

3. Results and discussion

3.1. Residual stress analysis

Additively manufactured components exhibit macroscopic (Type I) residual stresses. Layer-by-layer printing varies the stress fields due to misfit between adjacent regions, giving rise to non-uniform plastic deformation caused by steep thermal gradients.³¹ Table 2 lists the factors affecting the residual stress.

Residual stresses are classified according to their magnitude and nature and carry consequences for mechanical performance and structural integrity. As each new layer is formed, thermal misfit generates tensile stresses in the exterior regions and compressive stresses in the interior region (thermal gradient mechanism). The latter retards fatigue crack initiation and slows crack growth, while the former promotes crack nucleation and propagation under cyclic loading.

As noted by Withers³², tensile stresses raise the mean stress during the fatigue cycle, which in turn reduces the allowable stress amplitude (Goodman–Gerber relation), thereby affecting the fatigue life of the component and rendering it detrimental to structural applications. In contrast, compressive stresses prove to be beneficial for turbine applications by closing the surface and near-surface cracks, thereby increasing the threshold stress intensity factor required for crack initiation and propagation. Tensile residual stresses are significantly dominant in the as-built condition, as widely reported in the literature³³, while upon removal from the substrate plate, stress redistribution occurs, resulting in the formation of compressive stresses.

Figure 1 illustrates the residual stress plot. Compressive residual stresses, evidenced by the negative slope of $\sin^2\psi$, depict the nature of stress present in the specimen. This finding is consistent with earlier AM studies.³⁴ The stress tensor data acquired from as-built PBF-LB IN625 specimens revealed pronounced orientation-dependent anisotropy. The vertically oriented (90°) specimen

Table 1. Process parameters of powder bed fusion–laser-based IN625

Process parameters	Specification
Laser power	400 W
Laser type	Ytterbium green fiber laser
Scan speed	910 mm/s
Hatch space	0.11 mm
Layer thickness	60 μm
Inert gas	Nitrogen
Spot diameter	80 μm
Pre-heating temperature	80 $^{\circ}\text{C}$
Recoater blade (type)	Mild steel

Table 2. Factors affecting residual stresses

Process parameters	RS
Beam variables	
Power	\uparrow
Scan speed	\downarrow
Process conditions/geometry	
Layer thickness	\downarrow
Base plate heating	\downarrow
Part geometry	\uparrow
Scan strategy	
Beam re-scan	\downarrow magnitude
Dwell time	Affect RS magnitude
Scan rotation	Affect RS magnitude

Abbreviation: RS: Residual stress.

exhibited the highest compressive stresses (-665 MPa) along the build direction, arising from the steep thermal gradient and constrained heat dissipation inherent to vertical solidification.

Horizontally oriented specimens experience more uniform heat dissipation, whereas the combination of horizontal and vertical thermal effects leads to moderate residual stresses in 45° specimens. The thermal gradient and cool-down mechanisms are the two primary sources of residual stress that must be understood to determine the origin of residual stresses as a function of build orientation.³⁵ Moreover, the evolution of the stress profile across the three build orientations is primarily driven by the strain-hardening effect during layer solidification.³⁶

The heat conduction through the powder bed and build platform follows the order: $0^{\circ} > 45^{\circ} > 90^{\circ}$, as the contact area of the solidifying cross-section with the build plate decreases with increasing build orientation/angle. The

time required to print each layer also contributes to the development of residual stresses. Shorter scan lengths per layer in the 90° specimen result in reduced layer-cooling times, enhancing heat accumulation. The resulting steep thermal gradients between layers drive higher compressive residual stresses, in accordance with the temperature gradient mechanism.³⁷

In contrast, the asymmetric geometry and partial heat extraction conditions of 45° orientation result in the lowest compressive stress (-138 MPa) among the three orientations examined. The 0° orientation exhibited a slightly lower compressive stress (-637.6 MPa) than the vertical build, but higher shear components (e.g., $\sigma_{13} = 40.4$ MPa, $\sigma_{23} = 84.3$ MPa), reflecting the directional accumulation of lateral thermal stresses along the scan path. The longer layer duration in the horizontal orientation leads to prolonged thermal interaction, contributing to asymmetric stress evolution across the layer thickness.

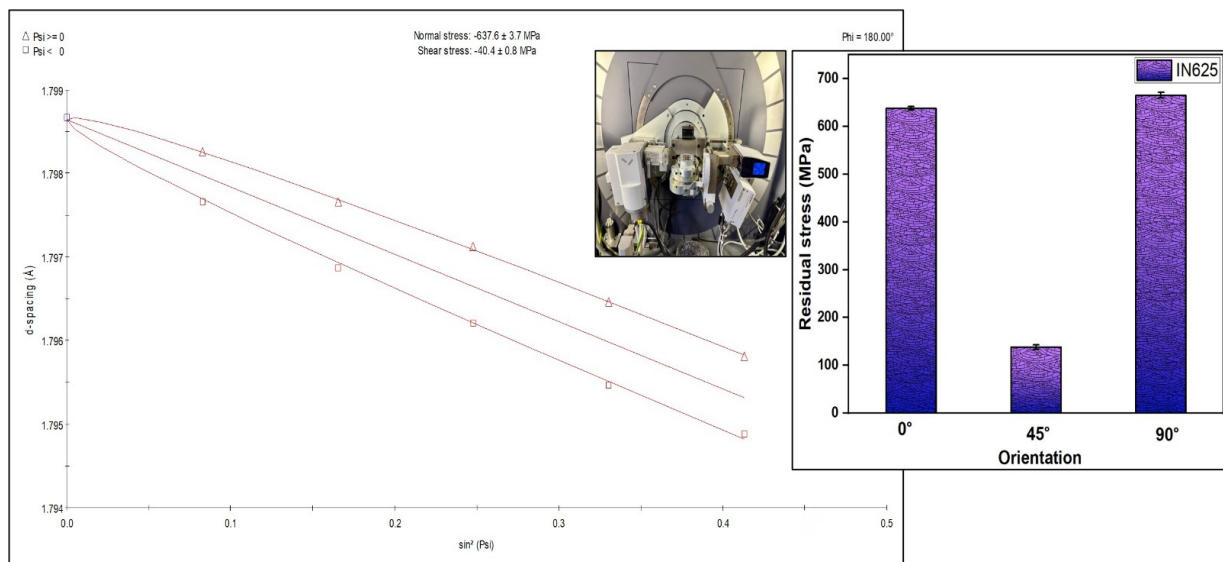


Figure 1. d-spacing versus $\sin^2\psi$ plot for the 0° orientation ($\phi = 180^\circ$) and histogram of orientation-dependent residual stress distribution for all three build orientations. The inset shows the X-ray diffraction measurement setup.

These findings confirm that heat flow direction and interlayer cooling time significantly influence the evolution of residual stresses in PBF-LB components.

3.2. Microstructural analysis: Grain structure/electron backscatter diffraction analysis

The microstructural results obtained via EBSD include the inverse pole figure (IPF), KAM, GND, and texture. A detailed analysis of the maps and their statistical distributions was conducted. The IPF reveals the crystallographic grain orientation across three build directions. A cluster of small grains was observed in the central/interior region of the 0° oriented printed sample. Conversely, many elongated columnar grains were detected in the 90° orientation. A steep thermal gradient is the principal driving force for the preferential growth of columnar grains during melt-pool solidification.³⁸

The formation of elongated columnar grains in the 90° build orientation during PBF-LB IN625 was predominantly influenced by the directional thermal gradients inherent to the AM process. According to classical directional solidification theory^{39,40}, a high thermal gradient-to-solidification rate ratio (G/R ratio) effectively suppresses constitutional undercooling, thereby favoring the continuation of epitaxial grain growth along the primary heat-extraction path. Under these conditions, the nucleation of new grains ahead of the solidification front is energetically unfavorable, and competitive growth mechanisms dominate. Consequently, crystallographically aligned grains grow preferentially along the thermal gradient, extending continuously across multiple layers to form a well-defined columnar microstructure. These

findings are consistent with the solidification models proposed by Kurz *et al.*⁴⁰ and Roebuck *et al.*⁴¹, wherein the absence of sufficient constitutional undercooling under high thermal gradients promotes the stabilization of columnar grains rather than facilitating a columnar-to-equiaxed transition.

As the grain size in EBSD is based on the criterion of orientation difference⁴¹, the grain size fractions for 0°, 45°, and 90° orientations were recorded as 5.08 ± 3.3 , 5.91 ± 3.29 , and 6.08 ± 3.29 , respectively. EBSD maps clearly illustrate distinct grain morphologies resulting from the different build orientations. Image quality maps, along with the corresponding IPF maps, delineate arc-shaped bands consistent with the morphology of overlapping melt pools formed during layer-by-layer solidification (Figure 2). The overlapping melt pools consist of elongated and columnar grains, with elongated grains easily identified across all three build orientations. The formation of these melt pools is a characteristic microstructural feature of PBF-LB materials.⁴²

During layer-by-layer printing in PBF-LB, directional solidification promotes grain growth aligned with the prevailing heat-flow direction.⁴³ It is widely recognized that the build direction is the most favorable as it aligns with the maximum thermal gradient.⁴⁴ Additionally, face-centered cubic (FCC) materials favor the $\langle 001 \rangle$ direction, as it possesses the lowest interfacial energy due to high atomic packing efficiency.

Although energy density varies with crystallographic orientation, grains tend to align along the $\langle 001 \rangle$ direction, developing a strong texture. Grains with orientations other

than $\langle 001 \rangle$ experience higher interfacial energy, making them less stable. Texture evolution, as indicated by the IPFs at 0° (Figure 2B), shows a high intensity in the $[001]$ plane along the build direction, as columnar grains grow epitaxially along the preferred axis (Figure 3A). Multiple random distributions corroborate the fiber texture, with its maximum value of 5.923.

Texture analysis was compiled for the three orientations using $\{001\}$, $\{111\}$, and $\{110\}$ pole figures. Figure 3B shows the pole figures for the three orientations. The 0° -oriented specimen exhibited four high-intensity spots along the principal axis in the $\{001\}$ pole figure, indicating cube texture. As solidification progresses, grains with strong $\langle 001 \rangle$ orientation dominate, attributed to grain formation during repeated heating and cooling, which depends on laser power. Texture development for the 45° specimen revealed rotation of the $\{001\}$ grains, aligning with its build orientation. Furthermore, the same rotation ($+45^\circ$) is observed for the 90° specimen. The 90° specimen exhibited dispersed intensity, along with the random grain spread observed in the $\{110\}$ plane. Conclusively, all three orientations exhibited a weak texture in the $\{110\}$ map, while the $\{001\}$ map consistently shows a strong texture. Moreover, each projected plane in the pole figure aligns with the $(100) \langle 001 \rangle$ orientation.

3.3. Orientation distribution function

Solidification and thermal gradient behavior influence texture development in AM.⁴⁵ Texture refers to the crystallographic orientation in polycrystalline materials and plays a significant role in determining the mechanical strength of additively manufactured components.^{46,47} It should be noted that processing parameters and build orientation determine the mechanical properties of structural components. Texture evolution as a function of build orientation was evaluated by constructing orientation distribution function plots from EBSD measurements. The three Euler angles ϕ_1 , ϕ , and ϕ_2 (as per Bunge convection) give the crystal rotation relating the crystallographic axes to the reference specimen axes. The ϕ_2 values 0° , 45° , and 65° were selected for analysis.

Generally, the FCC crystal structure possesses a Goss/cube texture, with partial shear textures. The major texture components observed in FCC metals exhibit $\langle 001 \rangle$ orientation growth. Figure 4A shows the cubic crystal system with standard orientation space highlighting the significant textures. The orientation distribution function plot shows Cube $\{110\} \langle 100 \rangle$, Goss $\{011\} \langle 100 \rangle$, brass $\{110\} \langle 112 \rangle$, and S $\{123\} \langle 634 \rangle$ textures. The 0° specimen exhibited predominantly cube texture with a slight presence of Goss, indicating recrystallization, whereas

shear texture is also prominent in the form of a rotated cube. Recrystallized components (cube texture) correlate with the highest strength observed in the horizontally oriented specimen (Figure 5). At $\phi_2 = 45^\circ$, a shift in texture components was observed. Partial recrystallization occurred due to brass and E and F shear textures. Rotated cube texture was also observed, attributed to the in-built presence of residual stresses, as reported by Subhendu *et al.*⁴⁸. In contrast, $\phi_2 = 65^\circ$ angle revealed a strong cube texture peak near the S component $(123) [634]$, representing shear-dominated deformation. This region, featuring the S component, reflects complex strain paths and local shearing phenomena occurring at melt pool boundaries in AM-processed IN625, where equiaxed grains form under thermal conditions.

3.4. Geometrically necessary dislocations and kernel average misorientation

Microstructural behavior plays a crucial role during plastic deformation. The two variants of dislocations during plastic deformation are GNDs and statistically stored dislocations. The GND density can be calculated using Equation 3^{49,50}:

$$\rho_{\text{GND}} = \frac{\beta \theta}{b \Delta x} \quad (3)$$

where β is a constant, θ represents KAM over distance x , and b is the Burgers vector.

The GND map and the GND density statistical map present the obtained values (Figure 6). An increase in dislocation density correlates with a reduction in grain size. GND maps reveal the spatial distribution of dislocation density. It was observed that the 0° oriented specimen exhibited the highest GND density. Statistical analysis validates this observation.

The 45° -oriented specimen exhibited low deformation and the lowest dislocation density of approximately $2.87 \times 10^{14} \text{ m}^{-2}$. As the grains rotated, the reduction in GND density for the vertically oriented (90°) specimen (approximately $3.25 \times 10^{14} \text{ m}^{-2}$) was moderate, consistent with the dislocation distribution. In addition, KAM represents the local lattice strain, which is relatively higher in horizontally oriented specimens. The level of strain distribution was analyzed using the KAM maps, providing insights into dislocation density. A high KAM intensity was observed in horizontally oriented specimens, contributing to increased dislocation-induced lattice distortion.

The EBSD-derived KAM and GND distributions provide crucial insights into the orientation-dependent strain accommodation mechanisms in PBF-LB IN625.

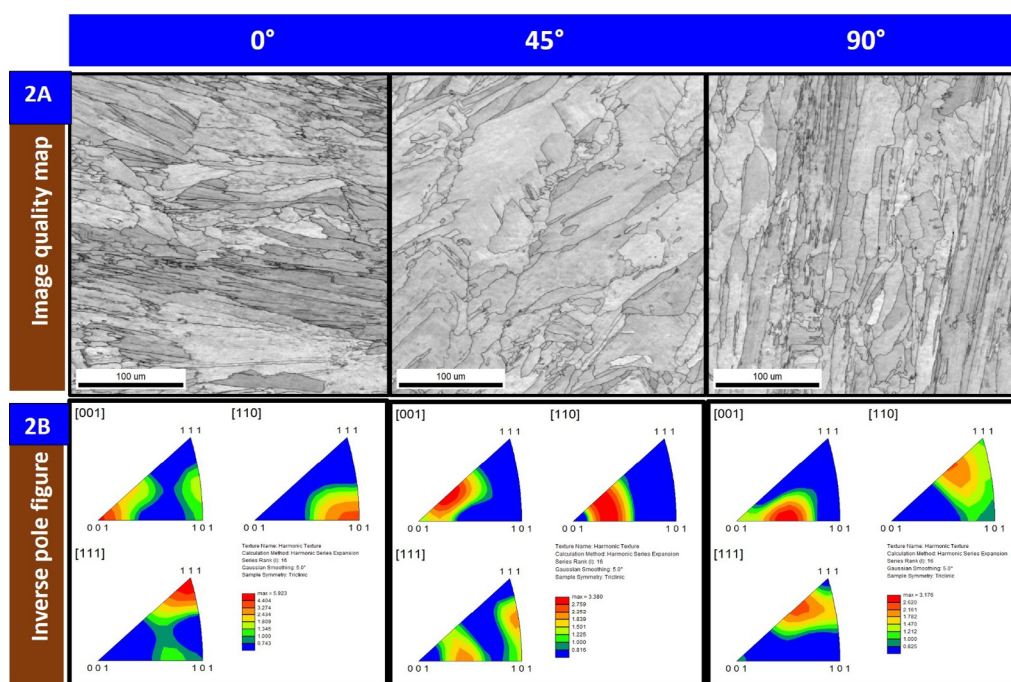


Figure 2. EBSD driven (A) image quality maps; (B) inverse pole figure maps corresponding to build orientation for 0°, 45°, 90°. The dominant red color represents grains growing consistently in the preferred direction, with microstructural evolution showing strong intensity toward the $\langle 001 \rangle$ crystallographic direction.

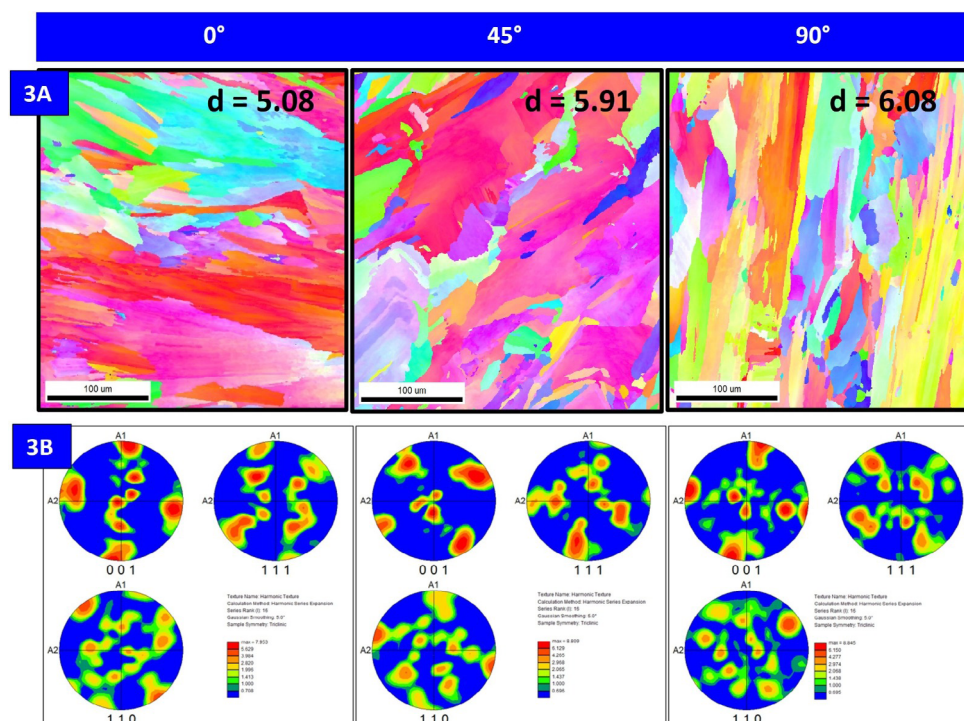


Figure 3. EBSD results of IN625. (A) Orientation image microscopy maps and (B) corresponding pole figure map for 0°, 45°, 90° build orientations.

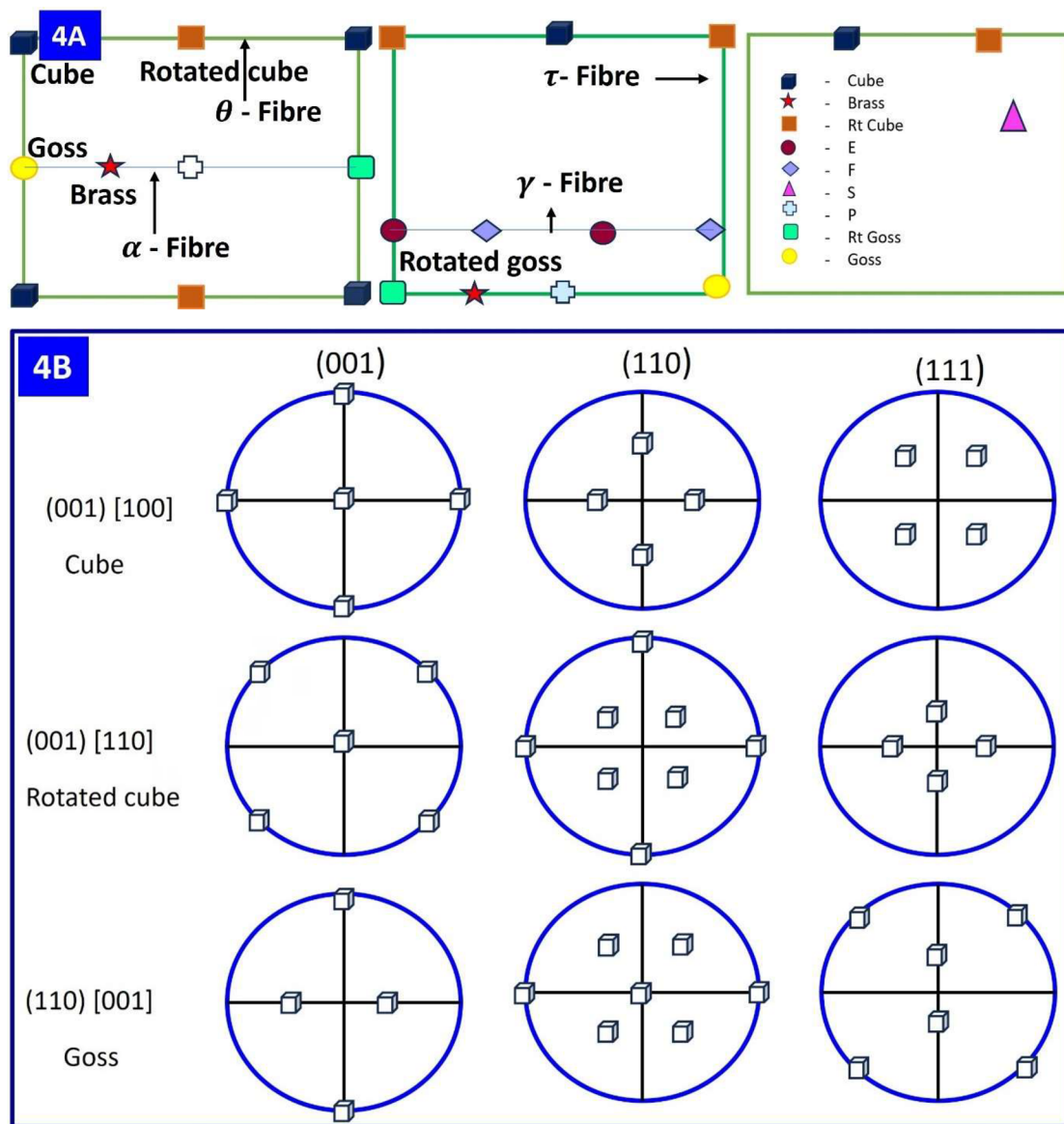


Figure 4. (A) Schematic showing the positions of major texture components in a face-centered cubic material and (B) standard orientation space illustrating the corresponding planes

Among the three analyzed build orientations, the 0° oriented specimen exhibited the highest KAM value and a corresponding GND density, recorded at $4.13 \times 10^{14} \text{ m}^{-2}$. This suggests substantial lattice curvature and a high GND density, primarily attributed to restricted dislocation mobility and accumulation near fine equiaxed grain boundaries. The dense grain boundary network in the horizontal build acts as a barrier to slip transmission, facilitating dislocation pile-up and resulting in local strain heterogeneity. These conditions are typical of the orientation that exhibits enhanced yield strength due to dislocation strengthening.

In contrast, the 45° orientation exhibited the lowest GND density (approximately $2.87 \times 10^{14} \text{ m}^{-2}$) and correspondingly reduced KAM intensity, indicating a more homogenized strain field and enhanced dynamic recovery during solidification. The oblique scan path and directional heat flow contribute to favorable thermal stress redistribution, leading to reduced defect accumulation. The 90° oriented specimens presented an intermediate GND value (approximately $3.25 \times 10^{14} \text{ m}^{-2}$) with columnar grains aligned parallel to the build direction. Although grain boundary obstruction to dislocation motion is reduced in this orientation, the vertical thermal gradient

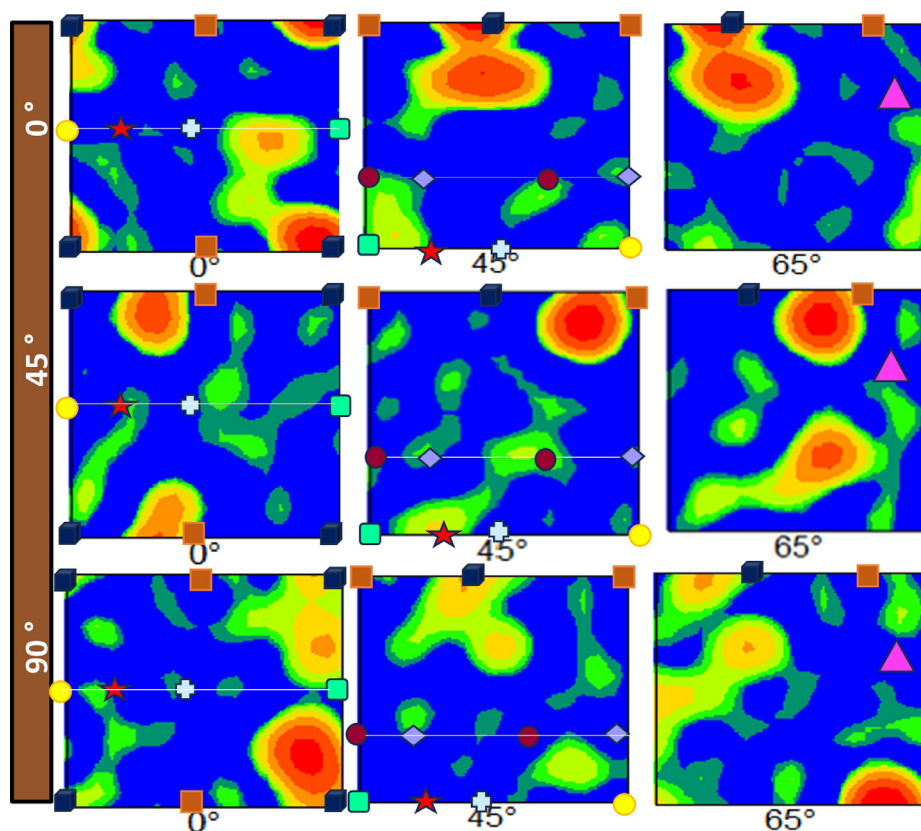


Figure 5. Orientation distribution function maps for the 0°, 45°, and 90° oriented specimens of powder bed fusion–laser-based IN625

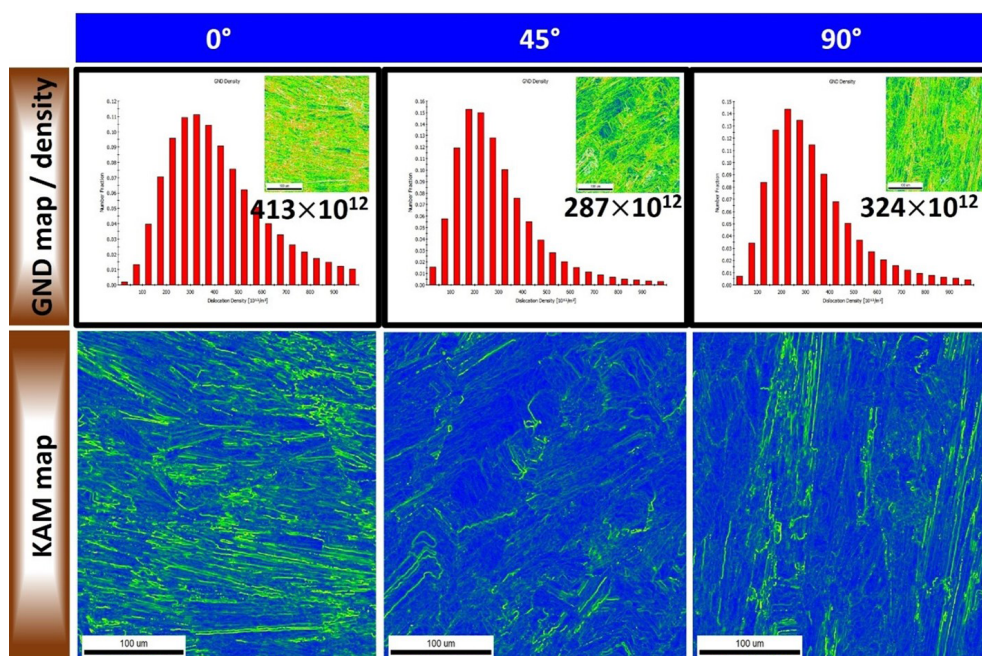


Figure 6. Geometrically necessary dislocation (GND) and kernel average misorientation (KAM) maps of powder bed fusion–laser-based IN625 for the 0°, 45° and 90° build orientations

induces measurable strain localization. In vertically built specimens, the reduced grain boundary density along the loading direction facilitates easier dislocation motion. This enhanced dislocation mobility increases ductility; however, it simultaneously lowers yield strength by reducing the material's resistance to plastic deformation.

3.5. Misorientation angle distribution

The distribution of misorientation angles determines the classification of grain boundaries. Figure 7 depicts the misorientation angle distribution for the three orientations. The quantitative grain boundary orientation was evaluated by classifying boundaries into low-angle grain boundaries (LAGBs) and high-angle grain boundaries (HAGBs). Here, grain boundaries with orientation angle $2\text{--}10^\circ$ (LAGB), whereas $10\text{--}180^\circ$ (HAGB).⁵¹ The average misorientation angle (θ) was determined to be 9.40° , which indicates a relatively uniform grain structure.

Furthermore, the LAGB map for the 0° oriented specimen showed the highest fraction of 0.244, compared to the 45° and 90° orientations. Grain boundary maps corroborated the dense LAGB network. In contrast, the 45° oriented specimen exhibited a more random grain boundary structure, with a significant shift toward higher misorientation angles. A heterogeneous grain structure was characterized by a fraction of 0.320 at larger angles and an average misorientation of 20.268° . This high-angle misorientation contributes to enhanced strain hardening. The HAGB fraction for this orientation was 0.58, the highest among the three orientations. The 90° oriented specimen demonstrated intermediate misorientation behavior, with a number fraction of 0.395 and an average misorientation of 16.5° .

3.6. Grain boundary character distribution and coincidence site lattice grain boundaries

In conjunction with misorientation angles, the grain boundary character distribution (GBCD) plays a crucial role in optimizing the mechanical properties of additively manufactured components. As shown in Figure 8, the GBCD of specimens with 0° , 45° , and 90° build orientations categorizes grain boundaries into LAGBs, HAGBs, and coincidence site lattice (CSL) boundaries. The rapid cooling and solidification characteristic of the PBF-LB process resulted in the 0° oriented specimen exhibiting a higher fraction of LAGBs, suggesting that dislocation substructures predominate. In contrast, specimens constructed with 45° and 90° orientations exhibited a higher proportion of HAGBs and CSL boundaries, which contribute to grain boundary stabilization and improved mechanical performance. Additionally, the distribution

of residual stress, mechanical strength, fatigue life, and corrosion resistance was significantly influenced by variations in boundary characteristics.⁵² Consequently, GBCD is critical in determining the most suitable build orientation.

Coincidence site lattice boundaries are particular grain boundaries in which the atomic lattices of two neighbouring grains align periodically. The CSL model describes grain boundary properties. The integer Σ reflects the reciprocal number density of lattice points that coincide in two adjacent grains.²⁷ Figure 8 shows that the predominant CSL bounds for the 0° orientation were $\Sigma 13b$, $\Sigma 25a$, and $\Sigma 19a$, whereas the average CSL fraction was 0.021, indicating a low CSL concentration. Low- Σ CSL boundaries improve material characteristics, including fatigue resistance, corrosion resistance, and creep strength. Furthermore, LAGBs are classified as $\Sigma 1$ CSL boundaries, in which all lattice points coincide precisely, resulting in minimal boundary energy. This enhances grain cohesion and reduces susceptibility to grain boundary sliding, reinforcing the material's structural integrity. As reported by Pleass *et al.*⁴⁹, PBF-LB IN625 does not show a significant preference in the statistical CSL plot.

3.7. Tensile behavior/mechanical response

The tensile response was measured for the as-built condition, which addresses the anisotropy based on build orientation, to determine the impact of build orientation on tensile behavior by examining specimens extracted from three different angles. Figure 9 depicts a histogram plot with three orientations: 0° , 45° , and 90° . The specimens printed parallel to the build plate (0° orientation) exhibited the highest ultimate tensile strength (963 MPa) and yield strength (727 MPa) while exhibiting low ductility. However, total elongation (%) was highest in the specimen printed perpendicular to the building plate (90°). The 90° -oriented specimen exhibited the largest elongation (54%), followed by those with 45° orientation. Meng *et al.*⁵³ also obtained similar results.⁵⁴ However, the 90° oriented specimen exhibited the lowest yield and tensile strengths. This inverse relationship arises from the presence of coarse columnar grains aligned with the build direction, which reduces grain boundary strengthening and limits resistance to dislocation motion.

Furthermore, elevated thermal exposure during printing facilitates dislocation annihilation, resulting in lower dislocation density and diminished strain-hardening capability. Consequently, the mechanical response is dominated by microstructural development rather than being strengthened by the high residual stress. However, these same factors enhance ductility, as

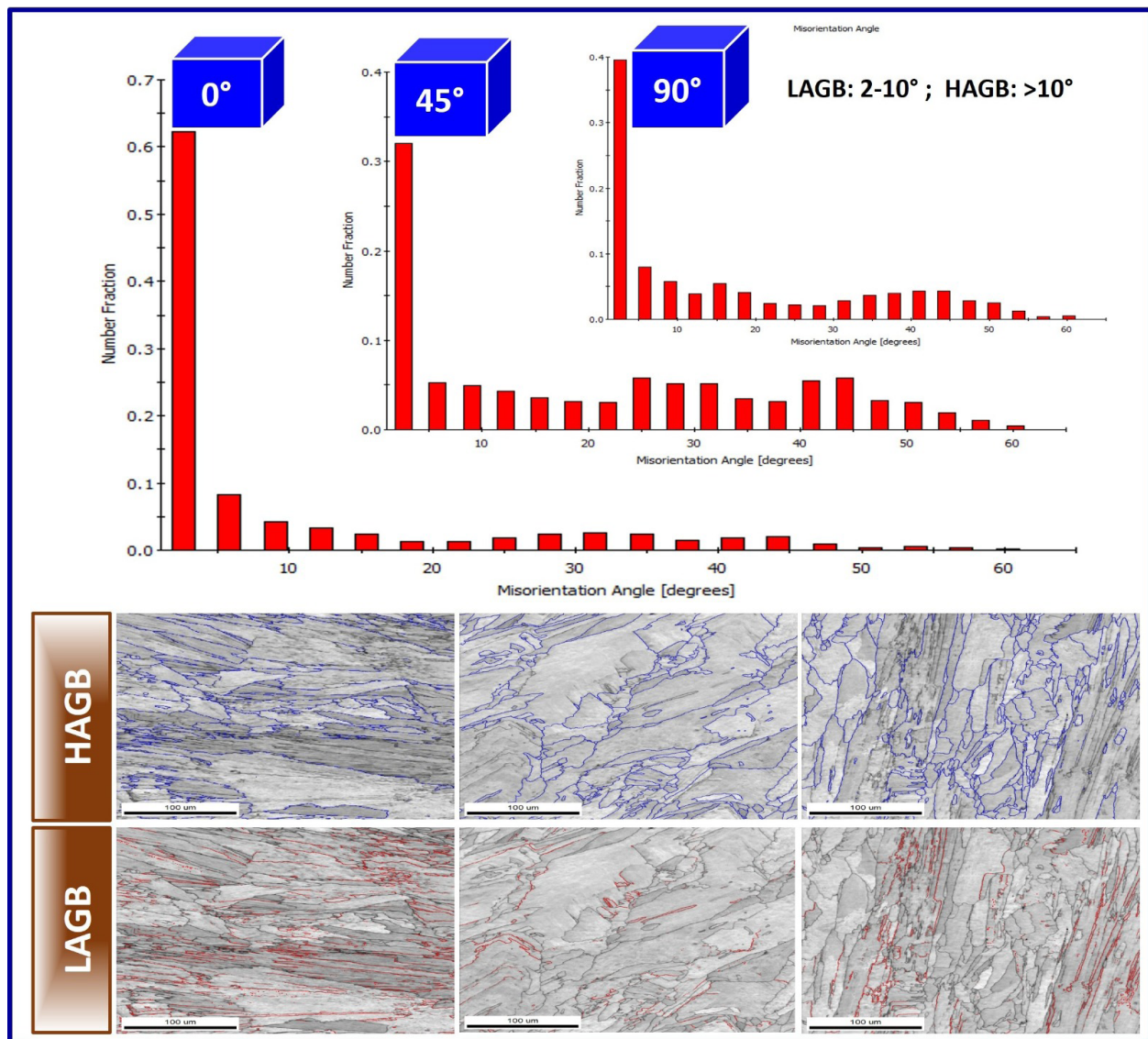


Figure 7. Misorientation angle distribution for the 0°, 45°, and 90° build orientations. Low-angle grain boundaries (LAGBs) and high-angle grain boundaries (HAGBs) are indicated by red and blue color codes, respectively.

fewer grain boundaries obstruct plastic flow, and larger grains accommodate greater elongation. This complex interplay highlights that residual stress alone does not dictate strength; instead, it must be evaluated alongside crystallographic orientation, grain morphology, and dislocation structure when assessing the performance of additively manufactured metals.

3.8. Fractography

Fracture morphologies of each specimen were examined using SEM. [Figure 10A-10A2](#) depicts the tensile fracture surface of a 0°-oriented specimen. [Figure 10B](#) shows the presence of cracks along with micro-voids. The specimens with the three orientations exhibit dimples of varying

sizes in high-magnification SEM images ([Figure 10A2](#), [10B2](#), and [10C2](#)), confirming ductile fracture. Tensile fractographs follow the sequence of crack initiation–voids/pores (lack of fusion)–dimples. Previous studies suggest that the high necking phenomenon is predominant in PBF-LB IN625.⁵⁵ Similar fractographic behavior has been reported in previous research.⁵⁶ [Figure 10B1](#) and [10B2](#) show void nucleation and coalescence. These cracks lead to areas of lack of fusion, acting as stress concentrators for crack initiation. A common feature of ductile materials is dimples, which result from micropore coalescence. Furthermore, the 90°-oriented specimen exhibited a large number of small, nested-type dimples distributed across its surface, indicating high ductility and a transgranular

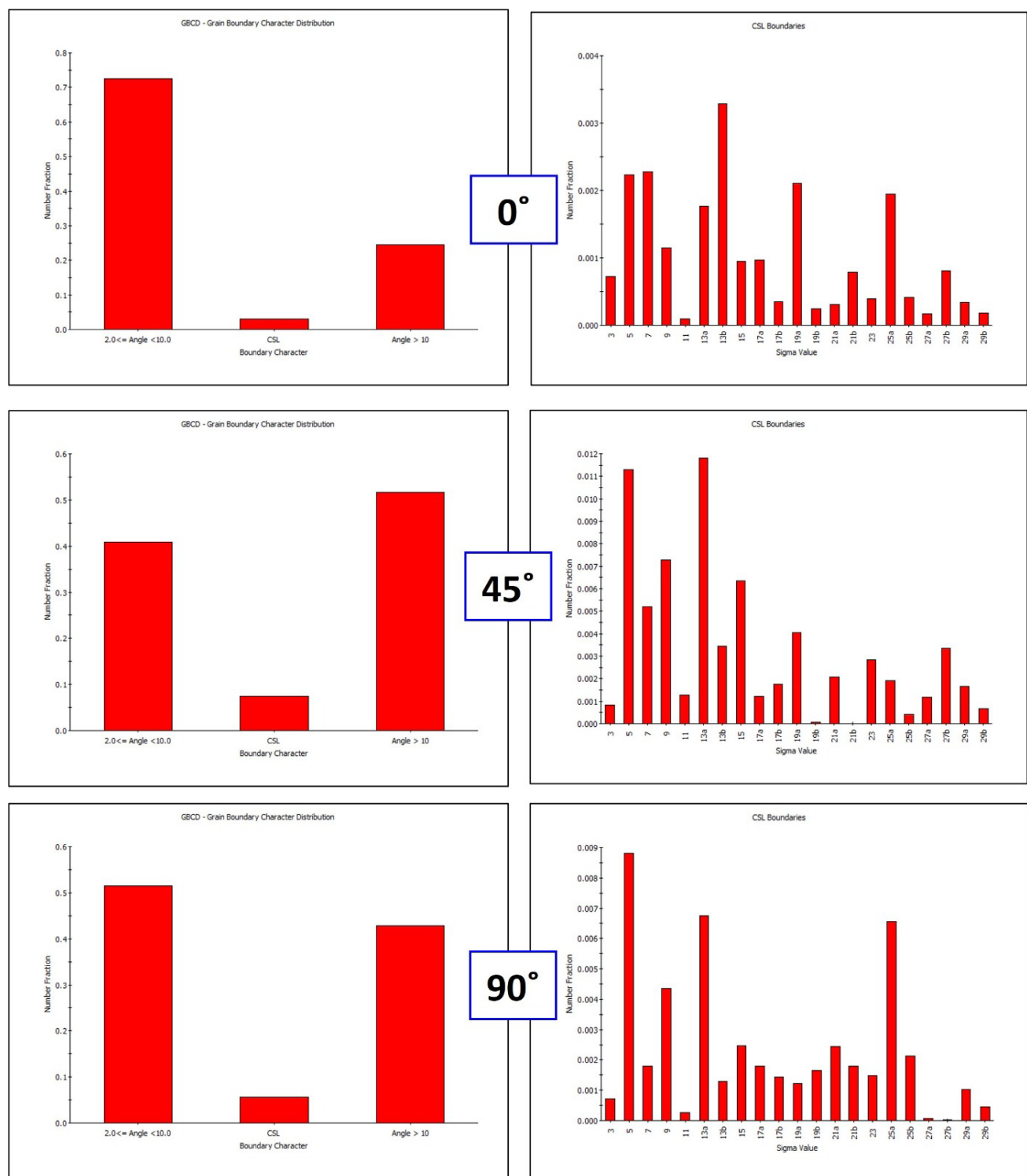


Figure 8. Grain boundary character distribution (GBCD) and coincidence site lattice (CSL) boundary fraction graphs for the 0°, 45°, and 90° build orientations

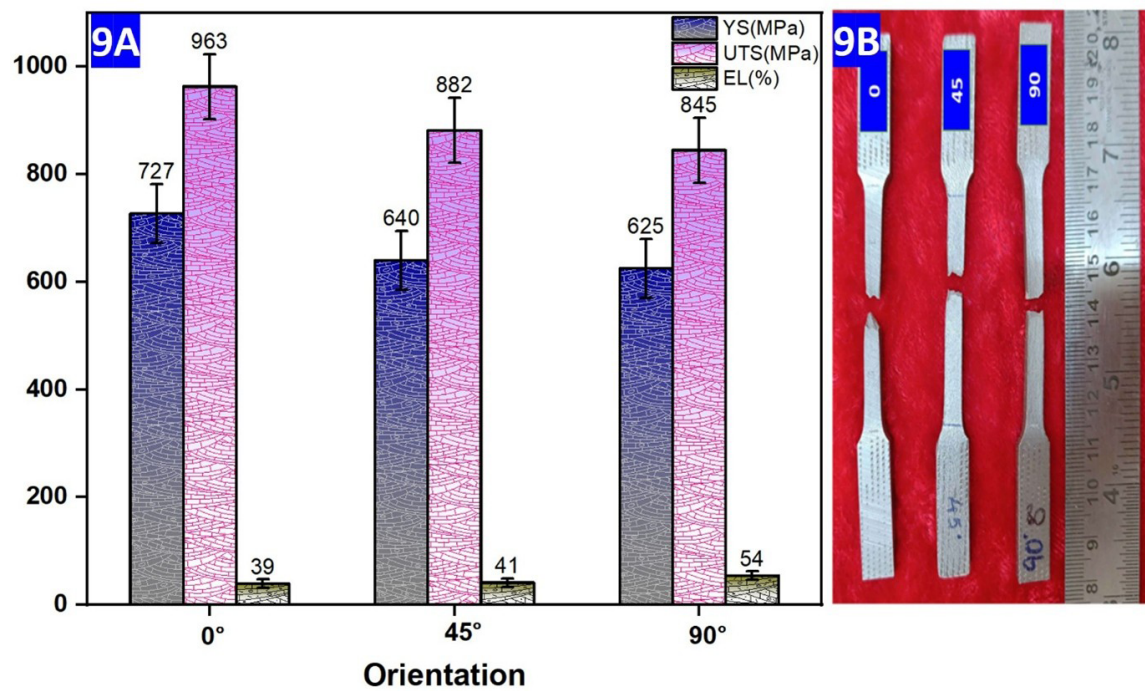


Figure 9. Mechanical response as a function of build orientation. (A) UTS, YS, and EL of as-built specimens for the three build orientations. (B) Fractured specimens.

Abbreviations: EL: Total elongation; UTS: Ultimate tensile strength; YS: Yield strength.

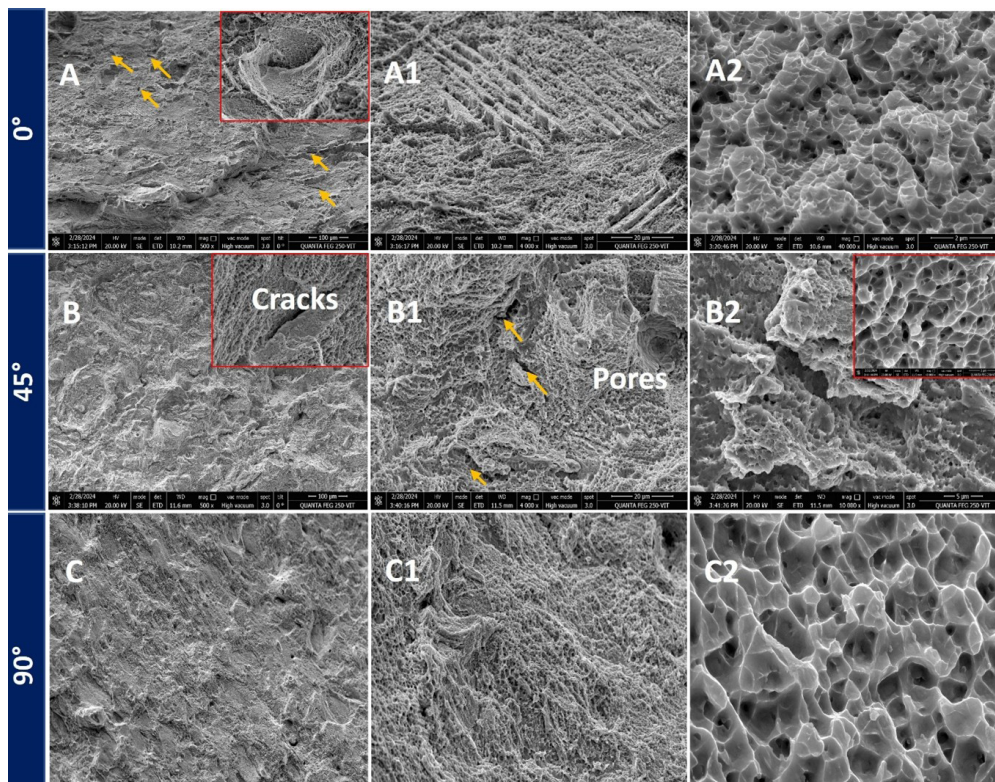


Figure 10. Scanning electron microscopy (SEM) fractographs of tensile specimens fabricated in the three build orientations: (A) 0°; (B) 45° (C); 90°. The yellow arrows indicate visible crack initiation and propagation sites.

fracture mode, demonstrating that cracks propagate through the grains. Moreover, inclusions within the dimple pits act as nucleation sites for micropores.

4. Conclusion

This study presents a systematic methodology for identifying the optimal build orientation for PBF-LB IN625, integrating EBSD-based texture analysis and residual-stress evaluation. The influence of build orientation on the thermal history, crystallographic texture, and mechanical response was critically examined and validated through experimental characterization. Among the orientations investigated, the vertically built (90°) specimen exhibited the highest compressive residual stress (−665 MPa), followed by the horizontal (0°; −636 MPa) and diagonal (45°; −138 MPa) specimens, establishing a clear orientation-dependent stress gradient. EBSD-derived KAM and GND density maps further elucidated the anisotropic deformation behavior. The 0° orientation depicted LAGBs, contributing to strain hardening through dislocation pile-up, while the 45° build offered moderate strength and ductility due to more uniform strain distribution. In contrast, the 90° orientation demonstrated enhanced ductility owing to reduced dislocation obstruction and higher fractions of HAGBs, as evidenced by its broader misorientation distribution. These orientation-specific microstructural features significantly influence the mechanical anisotropy of PBF-LB fabricated IN625. The achieved texture, particularly the presence of cube components, reflects the directionally dependent grain growth behavior governed by thermal gradients during solidification. The texture weakening at 45° coincides with reduced residual stress, and the 90° build re-establishes the cube texture while enhancing ductility. The 0° build tensile specimens exhibited the highest yield strength, showcasing a ductile mode of fracture. The novelty of this work lies in mapping the interdependence between thermal history, microstructural evolution, and mechanical behavior across build orientations under standardized processing conditions. These findings provide a foundational understanding of orientation-driven microstructural evolution and mechanical anisotropy in PBF-LB IN625, offering a pathway toward the qualification of additively manufactured components with tailored performance characteristics.

Acknowledgments

The authors are grateful to the Department of Science and Technology, New Delhi, India, for providing the financial support to acquire a laser powder bed fusion machine (EOS M290) through “Promotion of University and Scientific Excellence (PURSE)” under Grant No. SR/PURSE/2024/34 (TPN 56960) for carrying out work.

Funding

This study was supported by the Department of Science and Technology, New Delhi, India, under the “Promotion of University Research and Scientific Excellence (PURSE)” program (Grant No. SR/PURSE/2020/34 [TPN 56960]) for the procurement of a Direct Metal Laser Sintering machine (EOSM290 Machine)

Conflict of interest

The authors declare no conflict of interest.

Author contributions

Conceptualization: A. Raja Annamalai

Investigation: Sheeza Khan, A. Raja Annamalai

Methodology: A. Raja Annamalai, Sheeza Khan

Supervision: A. Raja Annamalai

Validation and formal analysis: Sheeza Khan

Writing—original draft: Sheeza Khan

Writing—review & editing: Sheeza Khan, A. Raja Annamalai

Ethics approval and consent to participate

Not applicable.

Consent for publication

Not applicable.

Availability of data

The data used in this work can be shared with the readers upon reasonable request via the corresponding author.

References

1. Bandyopadhyay A, Bose S. *Additive Manufacturing*. 3rd ed. CRC Press. 2025.
doi: 10.1201/9781003343868
2. Bourell DL. Perspectives on Additive Manufacturing. *Annu Rev Mater Res*. 2016;46(1):1-18.
doi: 10.1146/annurev-matsci-070115-031606
3. Herzog D, Seyda V, Wycisk E, Emmelmann C. Additive manufacturing of metals. *Acta Mater*. 2016;117:371-392.
doi: 10.1016/j.actamat.2016.07.019
4. Funch CV, Proust G. Laser-based additive manufacturing of refractory metals and their alloys: A review. *Addit Manuf*. 2024;94:104464.
doi: 10.1016/j.addma.2024.104464
5. Li Y, Lv H, Yuan Q, *et al*. High-temperature alloys: Recent advances from conventional alloys to complex concentrated systems. *J Mater Res Technol*. 2025;36:3298-3318.
doi: 10.1016/j.jmrt.2025.04.027

6. Bandyopadhyay A, Zhang Y, Bose S. Recent developments in metal additive manufacturing. *Curr Opin Chem Eng.* 2020;28:96-104.
doi: 10.1016/j.coche.2020.03.001
7. Tang H, Huang H, Liu C, Liu Z, Yan W. Multi-Scale modelling of structure-property relationship in additively manufactured metallic materials. *Int J Mech Sci.* 2021;194:106185.
doi: 10.1016/j.ijmecsci.2020.106185
8. Hariharan VS, Kaushik R, Murty BS, Phanikumar G. Effect of laser scan rotation on the microstructure and mechanical properties of laser powder bed fused Haynes 282. *Materialia.* 2024;33:101992.
doi: 10.1016/j.mtla.2023.101992
9. Zhong M, Liu W. Laser surface cladding: The state of the art and challenges. *Proc Inst Mech Eng Part C J Mech Eng Sci.* 2010;224(5):1041-1060.
doi: 10.1243/09544062JMES1782
10. Frazier WE. Metal Additive Manufacturing: A Review. *J Mater Eng Perform.* 2014;23(6):1917-1928.
doi: 10.1007/s11665-014-0958-z
11. Das A, Yadav V, AlMangour B, et al. Additive manufacturing of graphene reinforced 316L stainless steel composites with tailored microstructure and mechanical properties. *Mater Chem Phys.* 2023;303:127826.
doi: 10.1016/j.matchemphys.2023.127826
12. Singh UP, Shukla A, Swaminathan S, Phanikumar G. Effect of build orientations on residual stress, microstructure, and mechanical properties of additively manufactured alloy-718 components. *J Manuf Process.* 2024;113:1-15.
doi: 10.1016/j.jmapro.2024.01.047
13. Wei HL, Mazumder J, DebRoy T. Evolution of solidification texture during additive manufacturing. *Sci Rep.* 2015;5(1):16446.
doi: 10.1038/srep16446
14. Lee Y, Nordin M, Babu SS, Farson DE. Effect of Fluid Convection on Dendrite Arm Spacing in Laser Deposition. *Metall Mater Trans B.* 2014;45(4):1520-1529.
doi: 10.1007/s11663-014-0054-7
15. Pant P. *Residual Stress Distributions in Additively Manufactured Parts: Effect of Build Orientation.* Vol 1869. Linköping University Electronic Press. 2020.
doi: 10.3384/lic.diva-164108
16. Magana-Carranza R, Sutcliffe CJ, Patterson EA. The effect of processing parameters and material properties on residual forces induced in Laser Powder Bed Fusion (L-PBF). *Addit Manuf.* 2021;46:102192.
doi: 10.1016/j.addma.2021.102192
17. Mercelis P, Kruth J. Residual stresses in selective laser sintering and selective laser melting. *Rapid Prototyp J.* 2006;12(5):254-265.
doi: 10.1108/13552540610707013
18. Li C, Liu ZY, Fang XY, Guo YB. Residual Stress in Metal Additive Manufacturing. *Procedia CIRP.* 2018;71:348-353.
doi: 10.1016/j.procir.2018.05.039
19. Uddin Z, Butt MM, Kvvssn V, Salamci MU, Kizil H. Understanding the Effects of Manufacturing Attributes on Damage Tolerance of Additively Manufactured Parts and Exploring Synergy Among Process-Structure-Properties. A Comprehensive Review. *Eng Rep.* 2024:e13020.
doi: 10.1002/eng2.13020
20. Khairallah SA, Anderson AT, Rubenchik A, King WE. Laser powder-bed fusion additive manufacturing: Physics of complex melt flow and formation mechanisms of pores, spatter, and denudation zones. *Acta Mater.* 2016;108:36-45.
doi: 10.1016/j.actamat.2016.02.014
21. Carroll BE, Palmer TA, Beese AM. Anisotropic tensile behavior of Ti-6Al-4V components fabricated with directed energy deposition additive manufacturing. *Acta Mater.* 2015;87:309-320.
doi: 10.1016/j.actamat.2014.12.054
22. Marques A, Cunha Â, Silva MR, et al. Inconel 718 produced by laser powder bed fusion: an overview of the influence of processing parameters on microstructural and mechanical properties. *Int J Adv Manuf Technol.* 2022;121(9-10):5651-5675.
doi: 10.1007/s00170-022-09693-0
23. Courtright ZS, Venkatraman A, Yucel B, Adapa VSK, Diaz A, Kalidindi SR. High-throughput experiments and machine learning strategies for efficient exploration of additively manufactured Inconel 625. *Acta Mater.* 2025;288:120875.
doi: 10.1016/j.actamat.2025.120875
24. Sun SH, Koizumi Y, Saito T, et al. Electron beam additive manufacturing of Inconel 718 alloy rods: Impact of build direction on microstructure and high-temperature tensile properties. *Addit Manuf.* 2018;23:457-470.
doi: 10.1016/j.addma.2018.08.017
25. Shamsdini S, Pirgazi H, Ghoncheh MH, et al. A relationship between the build and texture orientation in tensile loading of the additively manufactured maraging steels. *Addit Manuf.* 2021;41:101954.
doi: 10.1016/j.addma.2021.101954
26. Kuo YL, Horikawa S, Kakehi K. Effects of build direction and heat treatment on creep properties of Ni-base superalloy built up by additive manufacturing. *Scr Mater.* 2017;129:74-78.

- doi: 10.1016/j.scriptamat.2016.10.035
27. Kalidindi SR, De Graef M. Materials Data Science: Current Status and Future Outlook. *Annu Rev Mater Res*. 2015;45(1):171-193.
doi: 10.1146/annurev-matsci-070214-020844
28. Munusamy S, J J. Effect of build orientation on the microstructure and mechanical properties of wire arc additive manufactured grade 91 steel/monel 400 bimetallic components. *Vacuum*. 2024;227:113429.
doi: 10.1016/j.vacuum.2024.113429
29. Nyssönen T, Gazder AA, Hielscher R, Niessen F. Habit plane determination from reconstructed parent phase orientation maps. *Acta Mater*. 2023;255:119035.
doi: 10.1016/j.actamat.2023.119035
30. Prevey PS. X-Ray Diffraction Residual Stress Techniques. In: Whan RE, ed. *Materials Characterization*. ASM International. 1986:380-392.
doi: 10.31399/asm.hb.v10.a0001761
31. Withers PJ, Bhadeshia HKDH. Residual stress. Part 1 – Measurement techniques. *Mater Sci Technol*. 2001;17(4):355-365.
doi: 10.1179/026708301101509980
32. Withers PJ. Residual stress and its role in failure. *Rep Prog Phys*. 2007;70(12):2211-2264.
doi: 10.1088/0034-4885/70/12/R04
33. Munusamy S, Jerald J. Microstructural Characterization, Residual Stress Evaluation and Deformation Behaviour of Wire Arc Additive Manufactured Grade 91 Steel and Monel 400 Bimetallic Components. *Met Mater Int*. 2025;31(8):2396-2416.
doi: 10.1007/s12540-025-01890-2
34. Sander G, Babu AP, Gao X, Jiang D, Birbilis N. On the effect of build orientation and residual stress on the corrosion of 316L stainless steel prepared by selective laser melting. *Corros Sci*. 2021;179:109149.
doi: 10.1016/j.corsci.2020.109149
35. Vishwakarma J, Chattopadhyay K, Santhi Srinivas NC. Effect of build orientation on microstructure and tensile behaviour of selectively laser melted M300 maraging steel. *Mater Sci Eng A*. 2020;798:140130.
doi: 10.1016/j.msea.2020.140130
36. Salmi A, Piscopo G, Atzeni E, Minetola P, Iuliano L. On the Effect of Part Orientation on Stress Distribution in AlSi10Mg Specimens Fabricated by Laser Powder Bed Fusion (L-PBF). *Procedia CIRP*. 2018;67:191-196.
doi: 10.1016/j.procir.2017.12.198
37. Bartlett JL, Li X. An overview of residual stresses in metal powder bed fusion. *Addit Manuf*. 2019;27:131-149.
doi: 10.1016/j.addma.2019.02.020
38. DebRoy T, Wei HL, Zuback JS, *et al*. Additive manufacturing of metallic components – Process, structure and properties. *Prog Mater Sci*. 2018;92:112-224.
doi: 10.1016/j.pmatsci.2017.10.001
39. Gäumann M, Trivedi R, Kurz W. Nucleation ahead of the advancing interface in directional solidification. *Mater Sci Eng A*. 1997;226-228:763-769.
doi: 10.1016/S0921-5093(97)80081-0
40. Kurz W, Bezençon C, Gäumann M. Columnar to equiaxed transition in solidification processing. *Sci Technol Adv Mater*. 2001;2(1):185-191.
doi: 10.1016/S1468-6996(01)00047-X
41. Roebuck B. Measurement of grain size and size distribution in engineering materials. *Mater Sci Technol*. 2000;16(10):1167-1174.
doi: 10.1179/026708300101506911
42. Kljestan N, Diaz Vallejo N, Huynh T, McWilliams BA, Sohn Y, Knezevic M. Flaw type and build orientation dependent tensile and creep strength of 316L stainless steel fabricated via laser powder bed fusion. *Mater Sci Eng A*. 2025;922:147671.
doi: 10.1016/j.msea.2024.147671
43. Tekumalla S, Selvarajou B, Raman S, Gao S, Seita M. The role of the solidification structure on orientation-dependent hardness in stainless steel 316L produced by laser powder bed fusion. *Mater Sci Eng A*. 2022;833:142493.
doi: 10.1016/j.msea.2021.142493
44. Wang X, Muñoz-Lerma JA, Sanchez-Mata O, Atabay SE, Attarian Shandiz M, Brochu M. Single-crystalline-like stainless steel 316L with different geometries fabricated by laser powder bed fusion. *Prog Addit Manuf*. 2020;5(1):41-49.
doi: 10.1007/s40964-020-00123-9
45. Park H, Mullin KM, Kumar V, Wander O, Pollock TM, Zhu Y. Resolving thermal gradients and solidification velocities during laser melting of a refractory alloy. *Addit Manuf*. 2025;105:104750.
doi: 10.1016/j.addma.2025.104750
46. Ishimoto T, Morita N, Ozasa R, *et al*. Superimpositional design of crystallographic textures and macroscopic shapes via metal additive manufacturing—Game-change in component design. *Acta Mater*. 2025;286:120709.
doi: 10.1016/j.actamat.2025.120709
47. Zhang BB, Tang YG, Mei QS, Li XY, Lu K. Inhibiting creep in nanograined alloys with stable grain boundary networks. *Science*. 2022;378(6620):659-663.
doi: 10.1126/science.abq7739
48. Naskar S, Suryakumar S, Panigrahi BB. Post-processing of Inconel 718 superalloy by Laser-based Powder Bed Fusion:

- Microstructures and properties evaluation. *Mater Sci Eng A*. 2025;921:147601.
doi: 10.1016/j.msea.2024.147601
49. Kishor G, Mugada KK, Mahto RP, Sivanandam A, Digavalli RK, Amirthalingam M. Constitutive modeling of high-temperature deformation, fracture mechanisms, and metallurgical study of WAAM-Deposited Inconel 625 alloy. *Eng Fail Anal*. 2025;171:109350.
doi: 10.1016/j.engfailanal.2025.109350
 50. Sun SJ, Tian YZ, Lin HR, Wang ZJ, Zhang ZF. Revisiting the role of prestrain history in the mechanical properties of ultrafine-grained CoCrFeMnNi high-entropy alloy. *Mater Sci Eng A*. 2021;801:140398.
doi: 10.1016/j.msea.2020.140398
 51. Li S, Guo C, Hao L, Kang Y, An Y. In-situ EBSD study of deformation behaviour of 600 MPa grade dual phase steel during uniaxial tensile tests. *Mater Sci Eng A*. 2019;759:624-632.
doi: 10.1016/j.msea.2019.05.083
 52. Pleass C, Jothi S, Krishnan M. Grain boundary and triple junction characteristics analytics of additive manufactured Inconel 625 superalloy using selective laser melting. *Mater Sci Eng A*. 2023;869:144744.
doi: 10.1016/j.msea.2023.144744
 53. Liu M, Wang Q, Cai Y, *et al*. Dependence on Manufacturing Directions of Tensile Behavior and Microstructure Evolution of Selective Laser Melting Manufactured Inconel 625. *J Mater Eng Perform*. 2023;32(16):7488-7500.
doi: 10.1007/s11665-022-07622-6
 54. Liu M, Wang Q, Cai Y, *et al*. Dependence on Manufacturing Directions of Tensile Behavior and Microstructure Evolution of Selective Laser Melting Manufactured Inconel 625. *J Mater Eng Perform*. 2023;32(16):7488-7500.
doi: 10.1007/s11665-022-07622-6
 55. Alam K, Kim K bong, Jeong JW, Kwon YT, Yang S. Investigation of the strength-ductility tradeoff and controlling Cr₂₃C₆ carbides in Inconel 625 super alloy using high pressure heat treatment. *J Alloys Compd*. 2025;1017:179032.
doi: 10.1016/j.jallcom.2025.179032
 56. Su Y, Dai Z, Yang T, Wang Y, Liang X, Wu X. Study on hot deformation behavior and strengthening mechanism of Inconel 625 deposited metal at high temperature. *J Mater Sci*. 2021;56(29):16745-16761.
doi: 10.1007/s10853-021-06357-4